Surface & Coatings Technology 437 (2022) 128328

Contents lists available at ScienceDirect

Surface & Coatings Technology

journal homepage: www.elsevier.com/locate/surfcoat

Full length article

The effect of Sr addition on the microstructure and corrosion behaviour of a Mg-Zn-Ca alloy

Jun Song, Yonghao Gao *, Chuming Liu, Zhiyong Chen

School of Materials Science and Engineering, Central South University, Changsha 410083, China

ARTICLE INFO

Keywords:
Magnesium alloy
Hydrogen evolution test
Electrochemical impedance spectroscopy
Microstructure characterization

ABSTRACT

The application of magnesium alloys is rather limited due to their poor corrosion resistance despite of their promising mechanical properties. Alloying is considered one of the most efficient methods to influence the corrosion susceptibility of Mg alloys either by altering the bulk microstructures or by changing the surface chemistries. In the present study, the effects of Sr addition on the microstructure and corrosion properties of a Mg-Zn-Ca alloy were studied. The microstructure characteristics of the alloys were investigated using optical microscopy, scanning electron microscopy, X-ray diffraction and X-ray photoelectron spectroscopy, while the corrosion properties were evaluated by hydrogen collection method and electrochemical techniques including potentiodynamic polarization and electrochemical impedance spectroscopy. The results indicate that Sr addition significantly deteriorates the corrosion performance of the Mg-Zn-Ca alloy mainly by forming more micro-galvanic couples due to the precipitation of the more populous secondary phase particles. The corrosion product film accumulated on the sample surface marginally affects the corrosion resistance, as their compactness is rather compromised as the immersion time is prolonged.

1. Introduction

As the lightest structural metals, magnesium alloys possess a good strength-to-weight ratio and excellent damping capacity [1,2]. Therefore, Mg alloys have seen vast applications in areas (e.g. automotive and aeronautical industry) where lightweighting is of increasing concern [3,4]. Apart from this, Mg alloys have also been demonstrated potential for applications as medical implants due to their benign biocompatibility and biodegradability as compared with those inert implants made of stainless steel and titanium alloys [5,6]. However, the usage of Mg alloys either as structural materials or as bioimplants lags far behind that has been expected, largely due to the widely criticized corrosion issue [7,8]. Mg possesses the lowest standard electrode potential (−2.37 V vs. SHE) of all the practical structural metals (e.g. Al, Ti, and Steel), which makes it susceptible to corrosion attack when it is externally connected with other metals or with the presence of interior microstructural discontinuities (like impurities, secondary phases, etc.) to form galvanic couples [9–12]. Therefore, such corrosion problem has to be addressed appropriately, if cannot be completely avoided, before a dramatic increase in the application of Mg can be realized.

Several strategies, including impurity control (Fe, Cu, Ni) [13], alloying [14], surface treatments [15,16], and their combinations [17,18], have been proposed to increase the corrosion resistance of Mg alloys. However, the effectiveness of these methods is far from satisfactory [19]. For example, all the externally applied surface coatings can only provide temporary protection to the magnesium substrate, and once the coatings have been damaged, the corrosion process is even accelerated as compared with those uncoated Mg [20,21]. Selecting the appropriate alloying elements to reduce the corrosion susceptibility of Mg has been an active research area, and many encouraging results have been reported. For example, a simplified binary Mg-Ca alloy exists a remarkably low corrosion rate (0.1 mm/y) in 3.5 wt% NaCl solution (compared to that of ultra-high-purity Mg, i.e. 0.3 mm/y), which is attributed to the protective surface film induced by Ca micro-alloying [22]. Inspired by such results, it seems that enhancing the protectiveness of the corrosion film through alloying is an effective way to improve the corrosion property [23]. However, the effect of alloying is much more complex due to the formation of secondary phase particles when the alloying contents exceed their solubility. Such secondary particles are normally nobler with respect to the surrounding α-Mg, which readily forms micro-galvanic couples that enhance the corrosion rate. On the other hand, the continuous network of secondary phases may inhibit

* Corresponding author.
E-mail addresses: gaoyonghao_009@163.com (Y. Gao), cmliu@csu.edu.cn (C. Liu), czysh@netease.com (Z. Chen).

https://doi.org/10.1016/j.surfcoat.2022.128328
Received 30 November 2021; Received in revised form 16 February 2022; Accepted 2 March 2022
Available online 7 March 2022

corrosion propagation and improve the corrosion resistance of Mg alloys. Therefore, a more detailed discussion needs to be adopted to explain the changes in corrosion resistance of Mg alloys after alloying.

Mg-Zn-Ca alloy has been developed as a potential biodegradable material because of the essentiality of Zn and Ca for physiological functioning [24,25]. Considerable efforts have been devoted towards lowering the degradation rate and enhancing the biocompatibility of the Mg-Zn-Ca alloys. Element Sr can stimulate osteoblast synthesis and inhibit bone resorption [26]. Therefore, Sr addition is expected to improve the biocompatibility of Mg alloys. However, the effect of Sr addition on the corrosion resistance of Mg alloys remains controversial. Many publications reported that addition of Sr would reduce the corrosion resistance of Mg alloy because of the formation of secondary phases [27]. However, Sr addition has also been reported to induce effects (like refined grains, improved network continuity and enhanced oxide films protectiveness) that are beneficial from the aspect of lowering the corrosion rate [28,29]. Therefore, it is of interest to study comprehensively the effect of Sr addition on the microstructure and corrosion performance of Mg-Zn-Ca alloy.

In the present study, appreciable amount of Sr was added to a Mg-Zn-Ca alloy, the resulting microstructure characteristics and corrosion performance of the alloys with and without Sr addition were comparatively studied in an attempt to identify the effect of Sr on the corrosion performance and microstructure characteristics of the Mg-Zn-Ca alloy.

2. Experimental procedure

2.1. Materials preparation

The raw materials including pure Mg (99.9 wt%), pure Zn granules (99.9 wt%), and Mg-30 wt% Ca, Mg-10 wt% Sr master alloys were used to prepare magnesium ingots with a nominal composition of Mg-1.0Zn-0.3Ca-xSr alloys (x = 0, 0.4 wt%). Pure Mg was melted in a crucible preheated at 400–500 °C before adding Zn and master alloys in the molten Mg. After all the raw materials were melted completely, the melt was heated to 720 °C, and stirred by purging argon gas into it for 6–10 min to allow the thorough mixture of all the alloying elements. Then the melt was kept stagnant for 25 min to allow settling and/or floatation of solid inclusions. Then the refined melt was cast at 680 °C into a steel mould preheated at 300 °C to get an ingot with a dimension of Φ 30 × 100 mm. During the whole process of melting and casting, the material was protected by a mixture gas comprising SF_6 (0.8 vol%) and CO_2 (99.2 vol%).

The actual chemical compositions of the ingots were determined using inductive coupled plasma analysis, and the results are tabulated in Table 1. The resulting Mg-0.95Zn-0.26Ca (wt%) and Mg-0.96Zn-0.24Ca-0.40Sr (wt%) alloys were designated as ZX10 and ZXJ100, respectively in the present study.

2.2. Microstructure characterization

The microstructure of the as-casted samples before and after the corrosion test was observed by the optical microscope (OLYMPUS, BX63) and a scanning electron microscope (SEM, TESCAN MIRA3). The as-cast samples were ground using SiC abrasive paper for microscopic observation. Afterwards, the polished surface was etched by a metallographic etchant comprising 4 vol% nitric acid and 96 vol% ethanol to reveal the distribution of the secondary phases. The area fraction of the secondary phases was calculated by analyzing at least three SEM images using Image-Pro plus software. The composition of the secondary phase was detected by an energy dispersive X-Ray spectroscopy (EDS, Oxford Instruments X-MAX 50) attachment in the SEM. Electron backscattered diffraction (EBSD, Oxford Instruments C-Nano) was conducted to study the grain size of the as-cast alloys.

The phase compositions of the samples were identified using a Rigaku Smart-Lab X-ray diffractometer with a Cu Kα radiation (λ = 0.154 nm). The samples were scanned under the Bragg Brentano (θ-2θ) geometry in the 2θ range of 20–80° with a step size of 0.02° and a scan rate of 3 deg/min. The obtained diffraction patterns were analyzed using MDI JADE software integrated with the ICDD powder diffraction file database.

X-ray photoelectron spectrometer (XPS, ThermoFisher-VG Scientific ESCALAB 250Xi) was used to investigate the chemical state of the specimens after 24 hours' immersion in the 0.1 M NaCl solution, and the XPS spectrum was collected using Al Kα radiation ($h\nu$ = 1486.6 eV) as the excitation source. Apart from the survey spectrum, high-resolution spectra for the Mg 1*s*, Zn 2*p*, Ca 2*p*, Sr 3*d*, C 1*s* as well as the O 1*s* orbitals was also individually collected within their respective binding energy ranges. The corresponding XPS spectra were processed using the Thermo Avantage software. The binding energy of the spectra was calibrated against the binding energy (BE) of the C 1*s* peak (284.8 eV). The Smart background function embedded in the Avantage software was selected for the background subtraction. The characteristic binding energy used to resolve the measured XPS spectra is compiled from the NIST Database and X-ray photoelectron spectroscopy handbook.

2.3. Immersion tests

The corrosion performance of the as-cast samples was evaluated by immersing the samples into a NaCl solution (0.1 mol/L) at ambient temperature while collecting the released gaseous hydrogen. The experimental design was firstly reported in the literature [30] and widely adopted afterwards. The samples for hydrogen evolution tests were cut into a dimension of 10 mm × 10 mm × 8 mm. All the samples were ground using SiC paper to 3500#, cleaned with ethanol, and dried in hot air for 2–3 min. The ratio of the sample surface to the solution volume was 0.026 cm^2/mL.

To observe the cross-section morphology after immersion, the samples were sealed in an epoxy resin immediately after soaking in a NaCl solution (0.1 mol/L) for different periods. The mounted samples were polished using refining SiC abrasive papers, rinsed with ethanol and finally dried in hot air. The cross-section morphology after corrosion was observed by an OM (OLYMPUS, BX63).

2.4. Electrochemical measurements

The corrosion process was also characterized by electrochemical techniques using an electrochemical test interface (WuHan CorrTest Instrument). A conventional three-electrode cell with the sample and a platinum plate served as the working and counter electrode, respectively, while a saturated Hg_2Cl_2/Hg electrode was applied to provide a potential reference. A solution comprising 0.1 mol/L NaCl was prepared as the electrolyte, and the sample was exposed to the corrosive media with an area of 1 cm^2. To ensure the reliability of the results, each experiment was repeated at least three times. Firstly, the samples were immersed in the cell and their corresponding open circuit potential (OCP) evolutions with immersion time were recorded to provide a direct comparison of the corrosion tendency of the ZX10 and ZXJ100 samples.

Table 1
Chemical composition of Mg-Zn-Ca and Mg-Zn-Ca-Sr Alloy (wt%).

Element	Mg	Zn	Ca	Sr	Fe	Co	Ni	Cu	Si
Mg-Zn-Ca	*Bal.*	0.95	0.26	–	0.0027	<0.0001	<0.0001	0.0004	0.0062
Mg-Zn-Ca -Sr	*Bal.*	0.96	0.24	0.4	0.0029	–	0.0002	0.0003	0.0038

Then the corrosion performance of the two samples was studied using the potentiodynamic polarization (PDP) technique. The PDP test was conducted after immersing the sample in the cell for 12 h to get the OCP value stabilized, i.e., the changes of the OCP value were less than 10 mV over a time span of 10 min. In the PDP test, the potential was scanned from −0.4 V to +0.4 V (vs. OCP) at a rate of 1 mV/s. The electrochemical impedance spectroscopy (EIS) measurements were conducted every 6 h during the immersion process by applying a sinusoidal perturbation with an amplitude of 8 mV and a sweep frequency from 10^5 to 10^{-2} Hz. The resulting spectra were analyzed using the ZView software package.

3. Results

3.1. Microstructure characterization

The SEM images of the as-cast alloys are shown in Fig. 1 (a) and (b). It is clear that the microstructure of the as-cast ZX10 alloy consists of two typical characteristics, i.e., α-Mg matrix and secondary phase particles that are sparsely distributed either within the α-Mg grains or along the grain boundaries (Fig. 1 (a)). The volume fraction of the secondary phase is about 0.43% in the ZX10 alloy. With an addition of Sr into the ZX10 alloy, more secondary phases precipitated along the grain boundaries and in the grain interiors. To be specific, the volume fraction of the secondary phase is increased to approximately 1.76%. The EBSD results of the studied alloys are depicted in Fig. 1 (c) and (d). It is clear that the addition of Sr in the ZX10 alloy results in a refined average grain size that is determined to be roughly 248.6 μm and 186.1 μm, respectively, for the ZX10 and ZXJ100 alloy.

To identify the chemistry distribution within the alloys, EDX mapping analysis was also conducted, and the results are shown in Fig. 2. There are two eutectic products in the ZX10 alloy: 1) α-Mg phase + Zn & Ca-rich phase + Ca-rich phase, 2) α-Mg phase + Zn & Ca-rich phase, and the Zn & Ca-rich phase can either precipitate alone, or wrap around the Ca-rich phase (Fig. 2 (a)). As represented in Fig. 2 (b), a new phase (Sr-rich phase) precipitates in the ZXJ100 alloy due to the addition of the Sr, leading to an enriched phase category, i.e., 3) Sr-rich phase + α-Mg phase, 4) Sr-rich phase + (α-Mg phase + Zn & Ca-rich phase), 5) Sr-rich phase + (α-Mg phase + Zn & Ca-rich phase + Ca-rich phase).

To rationalize the presence of those secondary phases, thermodynamic calculation was conducted using the Pandat database, and the results are shown in Fig. 3. In the solidification process, α-Mg phase is first formed as the temperature decreases from the liquidous region. Then when the temperature is reduced to 404 °C, eutectic reaction takes place, leading to the formation of the ternary phase ($Ca_2Mg_5Zn_5$-IM1) (Fig. 3 (a)). Fig. 3 (b) shows the Scheil solidification curve of the ZXJ100 alloy, from which it is clear that the solidification of the alloy is accompanied by the formation of the $Mg_{17}Sr_2$ phase and IM1, etc.

The chemical composition of the various secondary phases is studied using the EDS technique, and the results are shown in Fig. 4. It is clear that Mg_2Ca, $Ca_2Mg_6Zn_3$ secondary phases can be identified in the ZX10 alloy, while the additional $Mg_{17}Sr_2$ phase is observed in the ZXJ100 alloy. Moreover, the Mg_2Ca phase exhibits preferential precipitation closely adjacent to the $Ca_2Mg_6Zn_3$ phase. For example, Point I, F and D (Mg_2Ca phase) in Fig. 4 is even encapsulated by the $Ca_2Mg_6Zn_3$ phase (represented by the points E and H). The atomic ratio of Mg: Sr in the EDS results is around 10, which is appreciably higher than the stoichiometric ratio of 8.5 (in $Mg_{17}Sr_2$ phase). Such difference can be rationalized considering that the EDS results are inevitably affected by the surrounding α-Mg phase (that presents a very high content of Mg). However, the thermodynamic calculation results deviate from the experimental data in this work, which may be caused by the different atomic diffusion rates between the thermodynamic calculation and experimental conditions [31].

The XRD results of the as-cast alloys are displayed in Fig. 5. Apart from the dominant α-Mg phase, diffraction peak associated with the $Ca_2Mg_6Zn_3$ phase have been observed at $2\theta = 42.6°$, while the peaks at $2\theta = 33.8°$, and $35.3°$ are believed to be diffracted from the Mg_2Ca phase. The Sr-rich phase identified in the ZXJ100 alloy (Fig. 2 (b)) is further confirmed to be $Mg_{17}Sr_2$ as demonstrated by the diffraction peaks at $2\theta = 24°$, $31°$, $56°$, and $60°$ (Fig. 5).

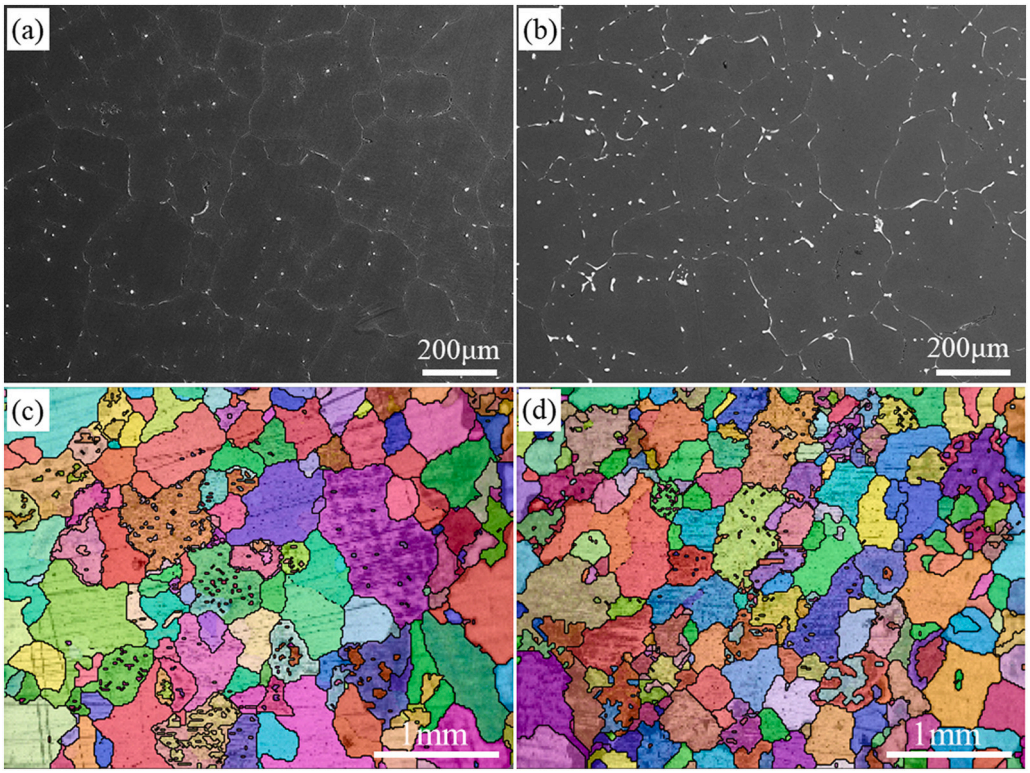

Fig. 1. The SEM images of the as-cast alloys: (a) ZX10 alloy; (b) ZXJ100 alloy; the EBSD inverse pose figures of the as-cast alloys: (c) ZX10 alloy, (d) ZXJ100 alloy.

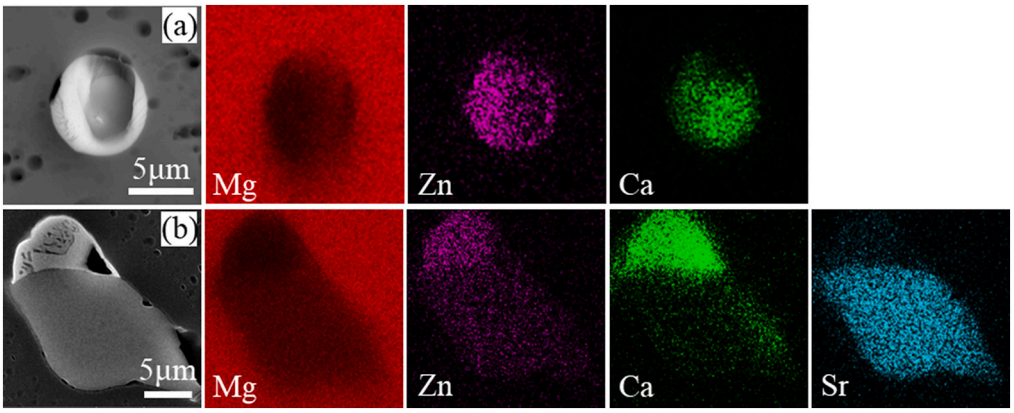

Fig. 2. The SEM images of the secondary phases and the distribution of its elements: (a) ZX10 alloy; (b) ZXJ100 alloy.

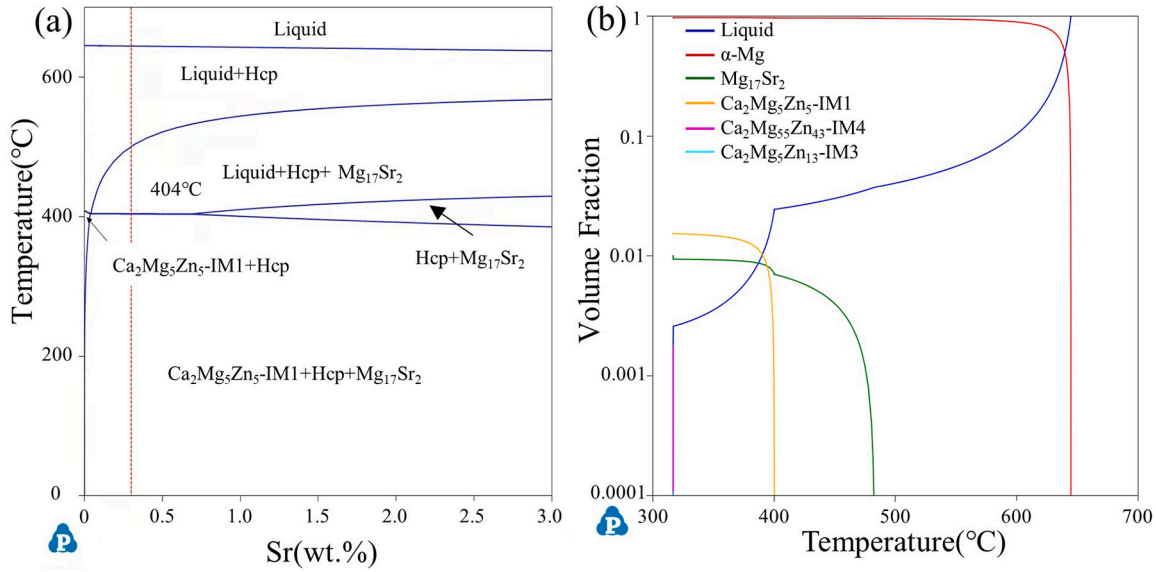

Fig. 3. Thermodynamic calculation of the target alloy: (a) phase diagram of quaternary Mg-1.0Zn-0.3Ca-Sr alloy; (b) the Scheil solidification curve of Mg-1.0Zn-0.3Ca-0.4Sr alloys.

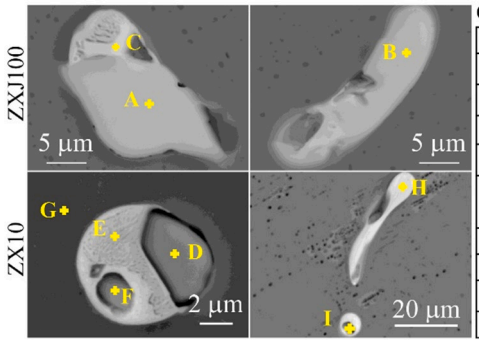

Chemical Compositions of the corresponding points (at.%)

Point	Mg	Zn	Ca	Sr	Phase Designation
A	85.1	5.6	1.0	8.2	$Mg_{17}Sr_2$
B	87.1	4.3	0.9	7.8	$Mg_{17}Sr_2$
C	69.8	14.3	14.6	1.2	$Ca_2Mg_6Zn_3$
D	67.4	5.0	27.6	-	Mg_2Ca
E	66.7	22.3	11.0	-	Two-phase eutectic structure $Ca_2Mg_6Zn_3$+α-Mg
F	67.4	14.6	18.0	-	Mg_2Ca
G	99.2	0.7	0.1	-	α-Mg
H	71.3	18.7	10.0	-	$Ca_2Mg_6Zn_3$
I	56.0	12.9	31.1	-	Mg_2Ca

Fig. 4. EDS analysis of the secondary phase particles of the as-cast alloys.

3.2. Immersion tests

3.2.1. Hydrogen evolution test

It has been widely documented that the corrosion of magnesium involves the following reaction [32]:

$$Mg(s) + 2H_2O(aq) = Mg(OH)_2(s) + H_2(g) \quad (1)$$

Theoretically, the consumption of 1 mol magnesium can release 1 mol hydrogen. Therefore, the corrosion rate of magnesium can be evaluated by measuring the released hydrogen [30].

Fig. 6 (a) presents the dependence of the accumulated hydrogen amount with immersion time. It is clear that both the curves gradually increase with immersion time, while the curve associated with the ZX10 alloy is well below that of the ZXJ100 alloy. The accumulated hydrogen

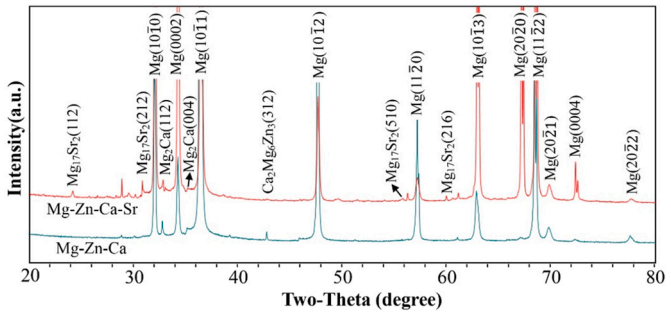

Fig. 5. X-ray diffraction (XRD) patterns of the as-cast alloys.

amount is around 0.69 ± 0.03 mL·cm^{-2} (0.22 mm/y) and 5.38 ± 0.37 mL·cm^{-2} (1.74 mm/y) for the ZX10 and ZXJ100 alloys, respectively, suggesting a higher corrosion rate of the ZXJ100 alloy. The evolution of the instantaneous hydrogen evolution rate (HER) during the immersion process is also obtained by derivative of the two curves in Fig. 6 (a) with respect to the immersion time, and the results are shown in Fig. 6 (b). The HER of the ZX10 alloy is significantly lower than that of the ZXJ100 alloy. Besides, the HER of the ZX10 alloy declines rapidly from 0.0065 mL·cm^{-2}·h^{-1} to 0.0040 mL·cm^{-2}·h^{-1} within the initial immersion stage up to 24 h, and then the curve has been flatted even when the immersion time extends to 168 h. However, the HER curve of the ZXJ100 alloy does not present any downward trend, rather the HER increases continuously albeit the slope of the HER curve decreases with immersion time. At the end of soaking, the HER curves of the two alloys remain stable, which might be attributed to the barrier effect of the accumulated corrosion product on the sample surface.

The different HER may be attributed to the differences in the micro-galvanic couples formed in the two alloys. Since the standard electrode potential of the $Mg_{17}Sr_2$ phase is nobler than that of the α-Mg phase [33], the newly formed $Mg_{17}Sr_2$ phase in the ZXJ100 alloy provides more micro-galvanic corrosion sites than that of ZX10 alloy, resulting in a higher corrosion rate.

3.2.2. *Corrosion morphology*

The SEM images after 24 hours' immersion in 0.1 M NaCl are shown in Fig. 7. It should be mentioned that the characteristics shown in Fig. 7 are quite common and the image presented was randomly captured from the alloys. The micro-corrosion sites (the black areas) initiate either at the grain boundaries or near the secondary phase, as indicated by the orange arrows in Fig. 7. In addition, the apparent boundary between the severely corroded area and the less corroded area (Fig. 7(a)) indicates that the corrosion process might be partially suppressed by the

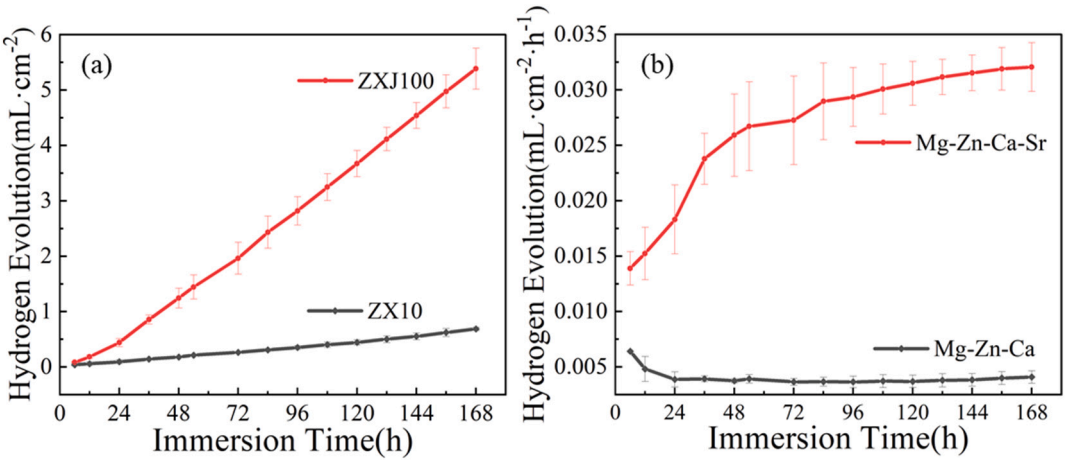

Fig. 6. (a) The evolution of the accumulated hydrogen amount; (b) the instant hydrogen evolution rate.

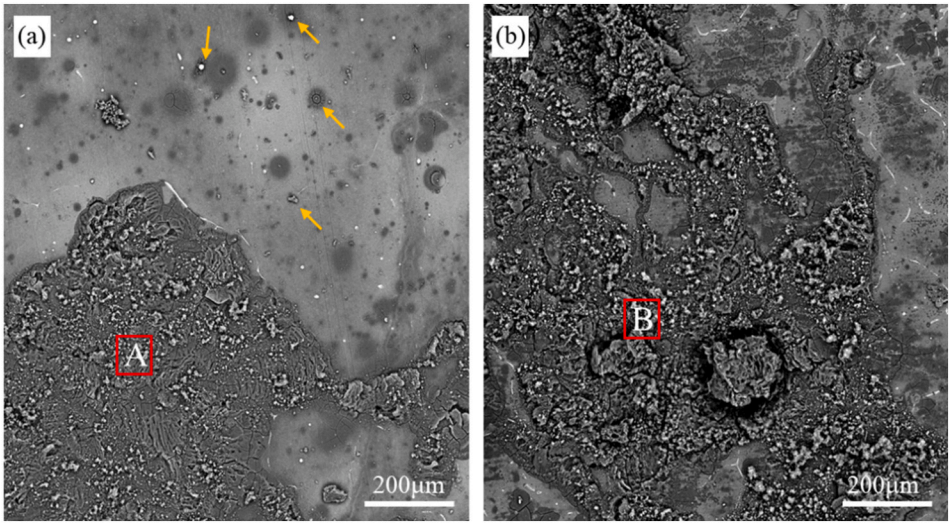

Fig. 7. The corrosion morphology soaked in 0.1 M NaCl for 24 h; (a) ZX10; (b) ZXJ100 (the yellow arrows representing the sites of the initial corrosion). (For interpretation of the references to colour in this figure legend, the reader is referred to the web version of this article.)

secondary phase network. Moreover, the larger area of corrosion product coverage on the ZXJ100 alloy as compared to that of the ZX10 alloy indicates a higher corrosion rate.

The surface chemical compositions after the corrosion test are studied using EDS, and the results are listed in Table 2. It is clear that the corrosion products are mainly comprised of Mg and O with a minor amount of Zn, regardless of the composition of the studied alloy. The content ratio of Mg/O is roughly 1/2, suggesting that the main corrosion product of the two alloys is $Mg(OH)_2$ following Eq. (1) and that reported in previous publications [8,34].

3.2.3. Cross-sectional observation after corrosion

The cross-sectional morphologies of the two samples after different immersion times are observed using optical microscopy and the results are shown in Fig. 8. A thin corrosion product film is accumulated on the sample surface, and its thickness varies with the immersion time. To be specific, the change of the corrosion product film thickness is not monotonous with increasing immersion time for the ZX10 alloy. The average corrosion product thickness on ZX10 alloy firstly decreases slightly from 5.9 ± 0.5 μm to 4.9 ± 0.9 μm when the immersion time is increased from 12 h to 24 h, and then it significantly increases to 11.3 ± 3.1 μm after 168 hours' immersion. The standard deviation of the average thickness also increases along with the immersion time. Therefore, it is clear that the non-uniformity of the corrosion product film becomes larger as the immersion time increases.

The corrosion product film thickness on the ZXJ100 alloy increases steadily with immersion time, and the resulting corrosion products layer is porous and presents significant roughness. An average film thickness of 7.7 ± 0.6 μm is measured from the ZXJ100 alloy after 12 hours' immersion, such value significantly increases to 12.3 ± 2.4 μm and 25.6 ± 9.0 μm when the immersion time increases to 24 h and 168 h, respectively. Apparently, the thickness of the corrosion product covering the ZXJ100 alloy is appreciably higher than that of the ZX10 alloy because more corrosion products have been formed due to the higher corrosion rate of the ZXJ100 alloy (Fig. 6).

3.2.4. Surface chemical analysis

After 24 hours' immersion in 0.1 M NaCl, the surface chemical analysis of the samples was conducted using XPS technique, and the results are shown in Fig. 9. It is clear that the samples mainly comprise Mg, Zn, Ca, O and C from the survey scan. The C1*s* peaks mainly arise from environmental contamination while handling the samples. The Sr signal is too weak to be detected in the XPS survey scan of the ZXJ100 alloy. Nevertheless, the Sr 3*d* spectra are significant in the narrow scan. Each narrow scan spectra have been deconvoluted to determine the corresponding valent states of the various elements. It is clear that one peak at the binding energy (BE) of 1302.7 eV yields sufficient fitting to the acquired Mg 1*s* spectra, suggesting that the observed Mg mainly exists as $Mg(OH)_2$ [35]. Doublet peaks with a distance of 23 eV on the binding energy scale can be deconvoluted to model the Zn 2*p* spin-orbit splitting peaks, i.e. Zn $2p_{3/2}$ (BE = 1021 eV) and Zn $2p_{1/2}$ (BE = 1044 eV). The intensity ratio of the two Zn 2*p* sub-peaks was constrained to be 2/1 in the deconvolution analysis. The characteristic binding energy (1044 eV) of the Zn $2p_{3/2}$ spin-orbit is associated with the metallic Zn. Similarly, the Ca 2*p* peak has been resolved to Ca $2p_{3/2}$ (BE = 348.02 eV) and Ca $2p_{1/2}$ (BE = 351.41 eV) peaks, suggesting that the Ca atoms are compounding with the chloride anions to form $CaCl_2$. To determine the chemical state of Sr within the superficial surface of the alloy after corrosion test, the Sr 3*d* peak was deconvoluted as well. Two sub-peaks associated with the Sr $3d_{5/2}$ (BE = 132.6 eV) and Sr $3d_{3/2}$ (BE = 134.6 eV) spin-orbits and their intensity ratio being Sr $3d_{5/2}$: Sr $3d_{3/2}$ = 0.69 are added to fitting the acquired Sr 3*d* spectra. The Sr on the sample surface mainly exists as SrO, as confirmed by the Sr $3d_{5/2}$ peak at a binding energy of 132.6 eV.

Therefore, it is concluded that in the corrosion process, the metallic elements Mg, Ca and Sr have been oxidized. Deconvolution analysis of the O 1*s* peak yields two sub-peaks at BE = 530.9 eV and BE = 531.5 eV, inferring the presence of $Mg(OH)_2$ [35] and carbonates [36], respectively, on the sample surface. Combining the above analysis, it can be concluded that the $Mg(OH)_2$ is the main corrosion product of our studied alloys.

Table 2
The chemical composition of the corroded regions A and B in Fig. 7 (at.%).

Region	O	Mg	Zn
A	65.9	33.7	0.4
B	66.6	33.3	0.1

3.3. Electrochemical measurements

3.3.1. Open circuit potential (OCP)

As depicted in Fig. 10 (a), the OCP curves of the alloys in the 0.1 M NaCl rise continuously, due to the accumulation of corrosion product on the sample surface [37]. At the end of the soaking time, the OCP of the ZXJ100 alloy is higher than that of the ZX10 alloy.

3.3.2. Potentiodynamic polarization (PDP)

The PDP curves of the alloys are shown in Fig. 10 (b), in which the ZXJ100 alloy possesses nobler corrosion potential than the ZX10 alloy (as consistent with the OCP curves). The presence of the more populous secondary phases in the ZXJ100 alloy might be responsible for the shift of the OCP value towards the positive direction as compared with that of the ZX10 alloy. The cathodic portions of the two PDP curves exhibit similar behaviour, indicating similar reactions involved during the cathodic polarization. However, the corresponding anodic polarization behaviour is slightly different. For example, when the ZX10 alloy is slightly polarized in the noble direction from the OCP, the resultant current density increases but at a small rate suggesting the passivation of the sample surface. When the sample is polarized by >0.15 V above the OCP value, the associated current density increases at a much higher rate, which is indicative of the breakdown/detachment of the passive film. A quite similar scenario is also observed from the positive polarization portion of the ZXJ100 alloy, even though the threshold potential for the passive film breakdown is much smaller, i.e. 0.06 V, above the OCP value. Therefore, it can be inferred that the initial passive film on the ZXJ100 alloy is less protective as compared with that formed on the ZX10 alloy. Anodic polarization curves of Mg and its alloys might be complicated due to the negative different effect (NDE) during the anodic oxidation process, which undermines the rationality of the Tafel extrapolation method. Therefore, the cathodic Tafel extrapolation was applied for analyzing experiment polarization curves according to the method illustrated in Ref. [38]. The cathodic Tafel extrapolation results are summarized in Table 3 and the current density of ZXJ100 alloy is apparently higher than that of ZX10 alloy, indicating a higher corrosion rate of ZXJ100 alloy. Nevertheless, by converting the corrosion current density to weight loss rate (mm/y), it is clear that the PDP technique provides a much lower rate as compared with that of the hydrogen evolution test. Such difference might be attributed to the oversimplified general corrosion assumption of the Tafel extrapolation method (the samples actually undergo localized corrosion).

3.3.3. Electrochemical impedance spectroscopy (EIS)

The corrosion process of the two alloys is also studied by collecting the electrochemical impedance spectroscopies after various immersion times in 0.1 M NaCl, and the corresponding results are displayed in Fig. 11. The Nyquist and Phase-Bode plots of the ZX10 alloy are respectively shown in Fig. 11 (a) and (b), while that of the ZXJ100 alloy are depicted in Fig. 11 (c) and (d). Regardless of the immersion time, two depressed capacitive loops can be differentiated in the first quadrant of the Nyquist plots of the ZX10 alloy (Fig. 11 (a)) and two maximum peaks can be identified from the Phase plots accordingly (Fig. 11 (b)), i.e., one

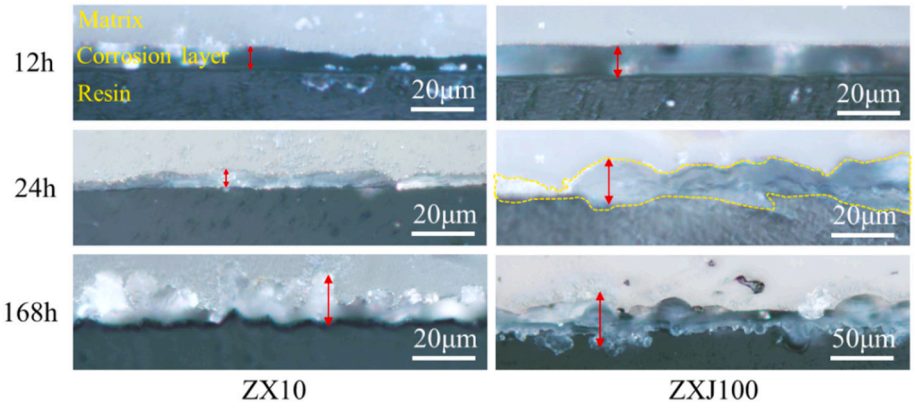

Fig. 8. The corrosion cross-section of investigated alloys with different immersion times.

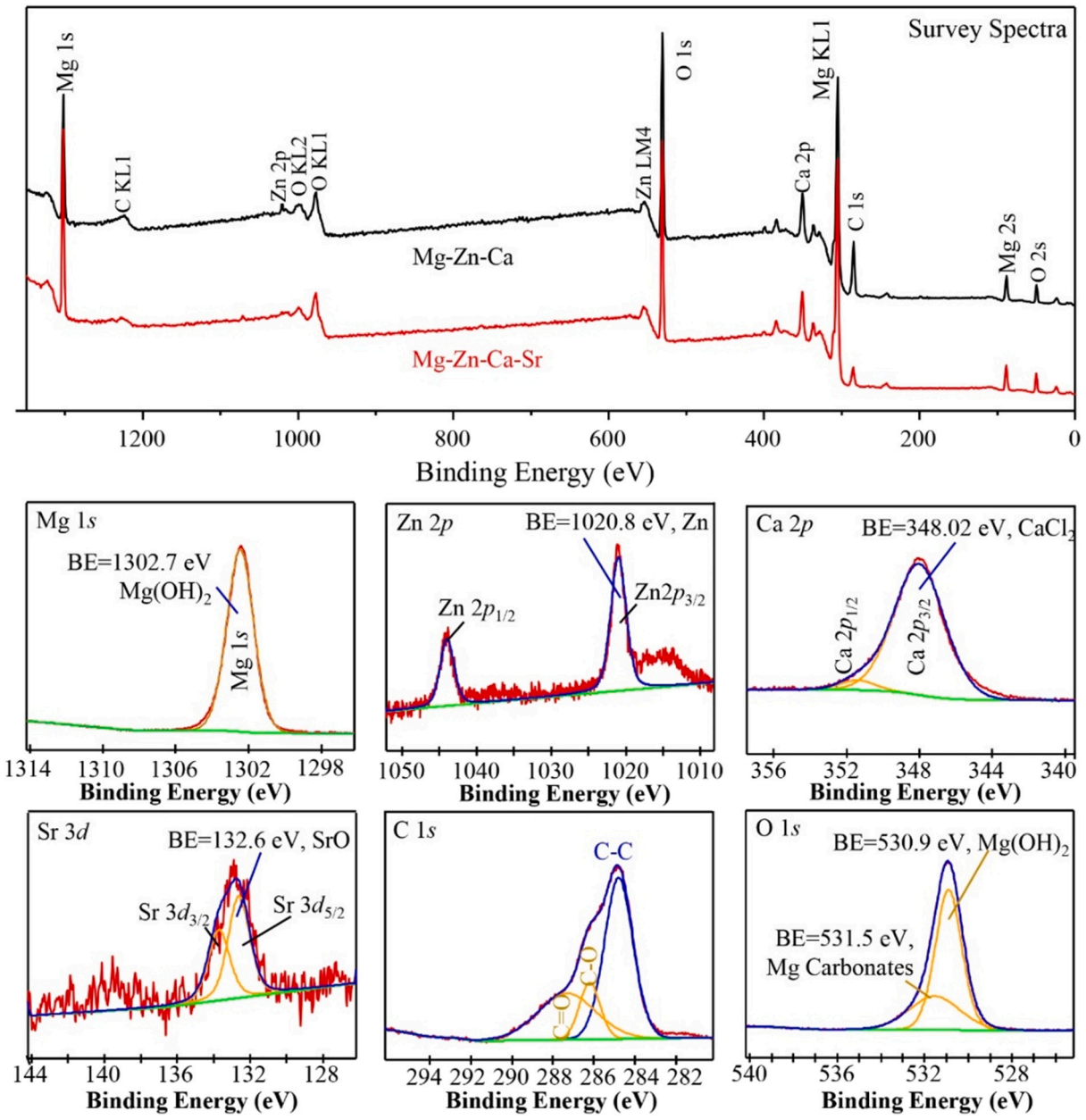

Fig. 9. The XPS survey scan of the two samples and the corresponding narrow scan of the ZXJ00 alloy after 24 hours' immersion in 0.1 M NaCl.

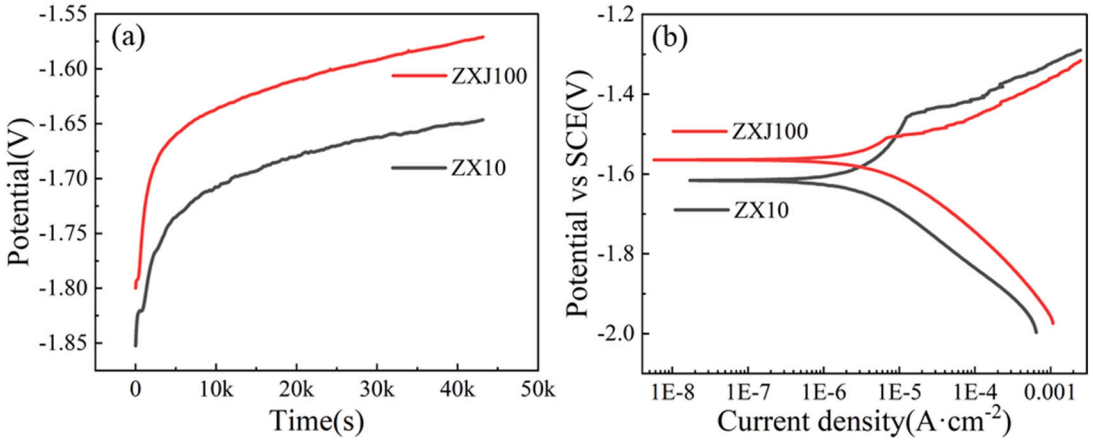

Fig. 10. The plot of (a) open circuit potential (OCP) and (b) potentiodynamic polarization.

Table 3
The cathodic Tafel extrapolation results obtained from potentiodynamic polarization curves.

Alloy composition	E_{corr} (V vs SCE)	i_{corr} (μA/cm^2)	P_i (mm/y)
ZX10	−1.62	3.11	0.07
ZXJ100	−1.56	10.70	0.24

in the higher frequency range of 10^4–10^0 Hz and the other within the lower range of 10^{-1}–10^{-2} Hz. Therefore, two separate processes with distinct time constants are expected to be involved in the corrosion process. In the high-frequency range, the first capacitive loop is attributed to the double layer at the electrode/electrolyte interface. The lower-frequency loop corresponds to the effect of the corrosion product covering the sample surface on the corrosion kinetics [39,40]. Nevertheless, the diameters of the corresponding loops increase monotonously as the immersion proceeds, indicating that the corrosion resistance of the ZX10 alloy has been improved in the corrosion process. This is corroborated by the rate of hydrogen evolution with immersion time shown in Fig. 6 (b). On the other hand, the phase peak in the higher frequency range has been shifted gradually towards the lower frequency range, which can be attributed to the accumulation of corrosion products [41,42].

The evolution of the EIS behaviour of the ZXJ100 alloy with the

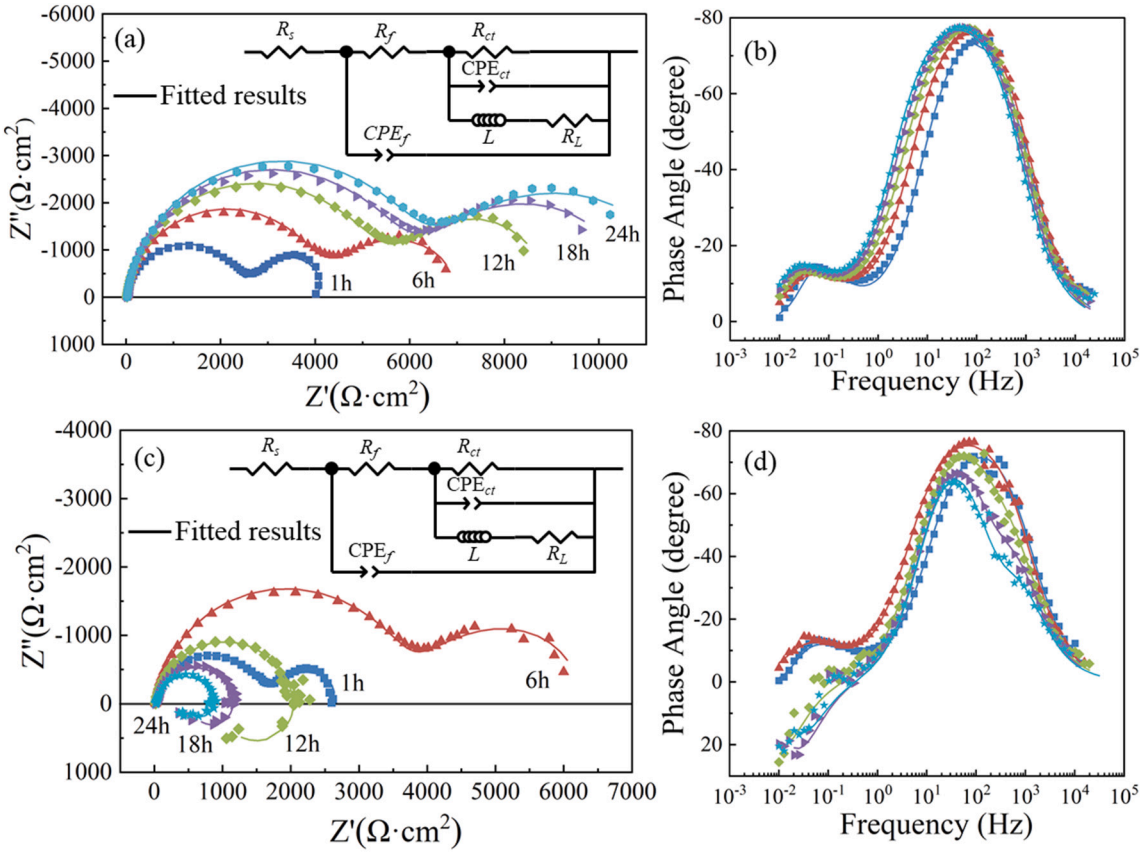

Fig. 11. Electrochemical impedance diagrams plotted after different soaking times in 0.1 M NaCl: (a) Nyquist plots of ZX10; (b) Bode Phase Angle of ZX10; (c) Nyquist plots of ZXJ100; (d) Bode Phase Angle of ZXJ100.

immersion time is different from that of the ZX10 alloy. When the ZXJ100 alloy is immersed in the 0.1 M NaCl for 1 h, an additional loop with positive imaginary values in the fourth quadrant of the Nyquist plot can be identified apart from the two capacitive loops in the first quadrant. It should be noted that the presence of a positive imaginary part is not uncommon in the corrosion process of magnesium alloys, and has been considered associated with the formation of monovalent Mg^{+} as an intermediate process before being corroded to the finalized Mg^{2+} cations [32,43,44].

However, when the immersion time increases to 6 h, the characteristics of the Nyquist plots change from two apparent aspects. Firstly, the diameters of depressed semi-circles witness a significant increase, suggesting an improvement of corrosion resistance. On the other hand, the characteristic positive imaginary part never appears, which is associated with the change of corrosion mechanisms, i.e., the attribution of the inductive effects raised from the adsorption of intermediate Mg^{+} might have been outweighed by the capacitive effects (of the double layer), if not had been completely suppressed [43,44]. When the immersion process is further prolonged to 12 h, it seems that the corrosion kinetics has been reversed during the corrosion process. The positive imaginary part of the Nyquist plot persists while only one capacitive loop can be identified. Furthermore, the Nyquist plot has shrunk a lot as compared with the Nyquist plots derived from the ZXJ100 alloy immersed for 6 h. Such feature of one capacitive loop plus one positive imaginary part of the Nyquist plots retains as the immersion times increase to 24 h albeit the diameter of the corresponding loops decreases continuously with the immersion time.

According to the cross-sectional observation (Fig. 8) and the EIS diagram characteristics (Fig. 11), the corresponding equivalent circuits (EC) are proposed to quantitatively interpret the acquired EIS diagram, as shown in Fig. 11 (a) and (c), respectively. In the equivalent circuit, R_s represents the solution resistance, R_{ct} and CPE_{ct} are used to represent the loop associated with the double layer in the high-frequency range. The inductive behaviour shown in Fig. 11 is represented by a series connection of R_L and L. The accumulation of corrosion product on the sample surface induces an additional capacitive behaviour in the medium frequency range, and it is reflected by the parallel connection of R_f and CPE_f in the EC diagram. It is worth mentioning that the capacitive behaviour is represented by the constant phase element (CPE) rather than the ideal capacitor because of the dispersion effect arising from the nonuniformity of the interface.

Using the proposed equivalent circuit, the experimental EIS diagram can be satisfactorily fitted, as shown by the solid lines in Fig. 11. The corresponding fitting parameters are shown in Table 4, the goodness-of-fit assessed by the χ^2 value is also included. It is clear that CPE_f-T has the same order of magnitude (10^{-5}) regardless of the exposure time.

4. Discussion

4.1. The effect of average grain size on corrosion behaviour

EBSD results have verified that Sr addition has led to a refined average grain size of the Mg-Zn-Ca alloy. It has been widely reported that the grain refinement is beneficial in terms of reducing corrosion rate of Mg alloys [45]. Nevertheless, the corrosion rate of the ZXJ100 alloy with finer grains is observed to be higher than that of the ZX10 alloy in the present study. Such observation suggests that the positive effects of grain size on the corrosion rate have been overwhelmed by other negative effects, like increased secondary phase particles after addition of Sr to the Mg-Zn-Ca alloy.

4.2. The effect of secondary phases on corrosion behaviour

The secondary phases within magnesium alloys have a significant influence on corrosion behaviour [46]. The sparse distribution of the eutectic phases within the grains allows the formation of localized galvanic couples, enhancing the corrosion rate of the alloys. The standard electrode potential of the different phases in the ZX10 alloy follows a decreasing order as Mg_2Ca < α-Mg < $Ca_2Mg_6Zn_3$ [47]. The micro-galvanic couples may be formed either (a) between Mg_2Ca and $Ca_2Mg_6Zn_3$ or (b) between α-Mg and $Ca_2Mg_6Zn_3$. (The couple between Mg_2Ca and α-Mg cannot be formed because the Mg_2Ca phase is encapsulated in the $Ca_2Mg_6Zn_3$ (Fig. 2), preventing α-Mg from direct contacting to Mg_2Ca). The potential difference in type (a) couple is larger than that in type (b), therefore, the corrosion initiates easier at sites of type (a) couple. In this regard, the Mg_2Ca should have been dissolved ahead of α-Mg during the corrosion process.

The volume fraction of the secondary phase is much higher in the ZXJ100 alloy, suggesting more galvanic couples can be formed in the ZXJ100 alloy. In this regard, higher corrosion rate is expected from the ZXJ100 alloy. Moreover, the formation and distribution of the additional $Mg_{17}Sr_2$ phase also attribute to the higher corrosion rate by forming additional galvanic couples (apart from the two types of couples mentioned above) between $Mg_{17}Sr_2$ and α-Mg [33].

4.3. The effect of corrosion product film on corrosion behaviour

The corrosion product film has been reported to affect the corrosion performance of the magnesium alloys depending on the porosity, thickness and chemistry of the film. Assuming that the thickness and the porosity of the corrosion film covering the sample surface are termed as d and α, respectively. If the sample surface exposed to the corrosive solution is A, then the capacitance, CPE_f-T, of the corrosion film is directly related to the film characteristics in the following way [48]:

$$CPE_f - T \propto \frac{\varepsilon_0 \varepsilon A(1-\alpha)}{d} \quad (2)$$

where ε_0 is vacuum permittivity, ε is the relative dielectric constant of

Table 4
The simulation results of investigated alloys with different immersion time.

Immersion Time	R_s /Ω·cm^2	R_f /Ω·cm^2	CPE_f-T /μΩ^{-1}cm^{-2}s^n	n_1	R_{ct} /Ω·cm^2	CPE_{ct}-T /μΩ^{-1}cm^{-2}s^n	n_2	L /H·cm^2	R_L /Ω·cm^2	χ^2
ZX-1 h	23.6	2499	10.9	0.93	2230	1540.1	0.85	45,000	5000	0.0032
ZX-6 h	21.2	4127	11.0	0.93	3608	999.2	0.73	29,325	1524	0.0010
ZX-12 h	22.3	5159	11.8	0.94	4267	950.0	0.52	59,954	6019	0.0009
ZX-18 h	22.8	5972	13.8	0.93	5838	913.6	0.74	64,422	3427	0.0010
ZX-24 h	23.2	6375	15.2	0.93	6031	897.8	0.77	23,614	1255	0.0012
ZXJ-1 h	17.8	1596	12.9	0.93	1607	1990.5	0.70	32,363	2402	0.0023
ZXJ-6 h	18.8	3747	13.5	0.93	3237	1215.5	0.74	20,450	1409	0.0026
ZXJ-12 h	19.5	266	15.8	0.92	1763	2.3	1.0	28,871	1100	0.0133
ZXJ-18 h	19.5	89	13.9	0.94	1043	9.6	0.99	7249	643	0.0138
ZXJ-24 h	20.1	52	13.8	0.95	796	15.7	0.99	6729	865	0.0155

the film layer.

Once the porous corrosion product film is formed in the corrosion process, the pores will be filled with the corrosive solution, and the collective resistance of those pores can then be computed as:

$$R_f = \rho \frac{d}{A\alpha} \tag{3}$$

where ρ is the conductivity of the corrosion solution filling in the pores, d is the depth of the pores and is roughly equal to the thickness of the corrosion product film, $A\alpha$ is the overall area of the pores. It can be concluded that the R_f and CPE$_f$-T included in the EC is dependent on the morphology of the corroded product film. It is clear that the product of $R_f \times$ CPE$_f$-T is positively proportional to $\frac{1-\alpha}{\alpha}$, which means that higher $R_f \times$ CPE$_f$-T normally reflects smaller film porosity α. In this regard and based on the data shown in Table 4, it can be predicted that the porosity of the corrosion film on the ZX10 alloy decreases gradually during immersion, while that of the ZXJ100 alloy decreases significantly in the first 6 hours' immersion before increasing when the sample is immersed for >6 h.

The polarization resistance R_p of the investigated alloys is defined as the difference in impedance between the solution resistance (when f approaches ∞) and the zero frequency resistance (when f approaches zero) [49]. When the frequency trends to zero, capacitive components of the circuit approach infinite impedance, and inductive components approach zero impedance [49]. The equivalent circuit can be simplified to derive the overall corrosion resistance (R_p):

$$R_p = \frac{R_L R_{ct}}{(R_L + R_{ct})} + R_f \tag{4}$$

According to the data tabulated in Table 4 and Eq. (4), R_p can be calculated and its variation with immersion time is plotted in Fig. 12 (a), from which the R_p is observed to steadily increase for the ZX10 alloy during immersion up to 24 h. As for the ZXJ100 alloy, R_p first increases at 0–6 h, then sharply decreases at 6–12 h, afterwards it remains almost constant. Both of the R_p curves are corroborated by the rate of hydrogen evolution with exposure time.

To study the contribution of the corrosion product film to the corrosion resistance in the immersion period, the evolution of the R_f/R_p ratio with time is calculated and the results are shown in Fig. 12 (b). The R_f/R_p ratio of the ZX10 alloy only declines marginally and remains above 0.5 in the whole immersion process up to 24 h. However, the R_f/R_p ratio of the ZXJ100 alloy keeps decreasing with immersion time. Its value slumps from 0.59 to 0.27 when immersion is extended from 6 h to 12 h, and it is further reduced to around 0.1 when the immersion time is increased to 24 h. The results indicate that the corrosion film covering the ZX10 surface plays a significant role in inhibiting the corrosion propagation, while that covering the ZXJ100 alloy rapidly reduces its inhibition effect with the increasing immersion time. It should be mentioned that it is the porosity of the corrosion films that affects their inhabitation behaviour because the tendency of the R_f/R_p evolution coincides well with that of the film porosity.

The overall effects of Sr addition on the microstructure and corrosion process of the Mg-Zn-Ca alloy are schematically summarized in Fig. 13. Sr addition mainly leads to two aspects in terms of microstructure alteration, i.e. refined grains and enhanced secondary precipitates, that induce opposite effects on the corrosion process. Even though the positive effects of the refined grains are not significant, the negative effects of the increased secondary phase fraction are profound. In the initial immersion stage, the micro-galvanic corrosion occurs preferentially near the secondary phases. And the more populous secondary phases in the ZXJ100 alloy provide much more corrosion initiation sites, resulting in its higher corrosion rate other than that of the ZX10 alloy. With the increment of the immersion time, the corrosion may gradually spread towards interior of the alloy and the corrosion product gradually accumulates on the sample surface to the whole surface.

The corrosion process leads gradual accumulation of the corrosion products on the sample surface that also affects the corrosion process. The corrosion product film is porous, and can only partially inhibit the corrosion propagation rate, of the ZX10 alloy in particular. Meanwhile, the magnesium matrix around the secondary phases may be preferentially degraded, resulting in the detachment of the secondary phases from the matrix. Therefore, the contribution of the corrosion product on inhibiting the corrosion process of the ZX10 alloy is higher than that of the ZXJ100 alloys.

5. Conclusions

In the present study, Mg-0.95Zn-0.25Ca-xSr (x = 0, 0.4 wt%) alloys were prepared through a general casting method. The effect of Sr addition on the microstructure characteristics and corrosion properties of the Mg-Zn-Ca alloy was systematically studied. Particular attention was focused on the influence of the secondary phases and the corrosion product films on the corrosion performance of the alloys. The main findings are as follows:

1) The microstructure of the ZX10 alloy comprises of α-Mg, Mg_2Ca phase, and $Ca_2Mg_6Zn_3$ phase, and the secondary phase mainly precipitated along the grain boundaries and in the grains. The addition of Sr led to the formation of an additional $Mg_{17}Sr_2$ phase as well as an increased volume fraction of the secondary phases.
2) The hydrogen evolution study and the EIS investigates results indicated that the addition of Sr deteriorated the corrosion resistance of

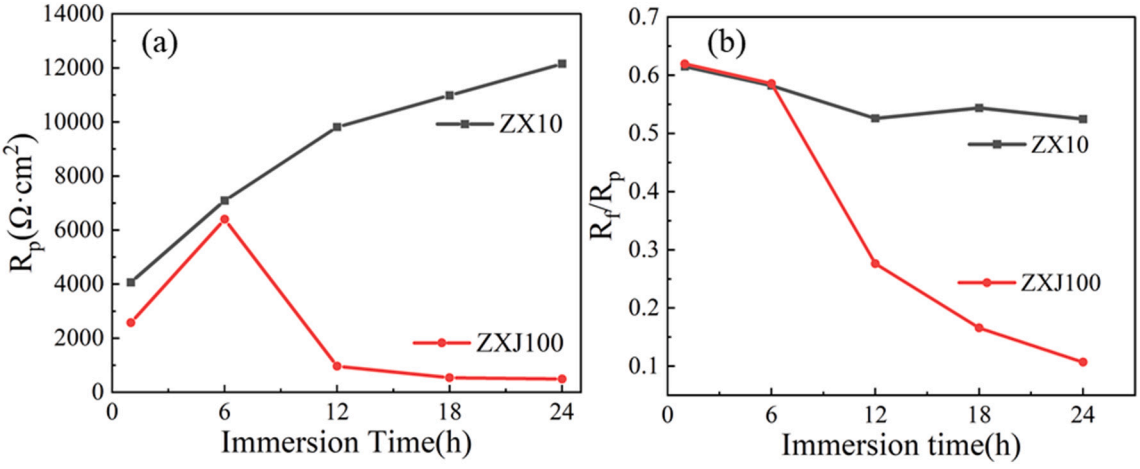

Fig. 12. (a) The evolution of the corrosion resistance and (b) R_f/R_p ratio with immersion time.

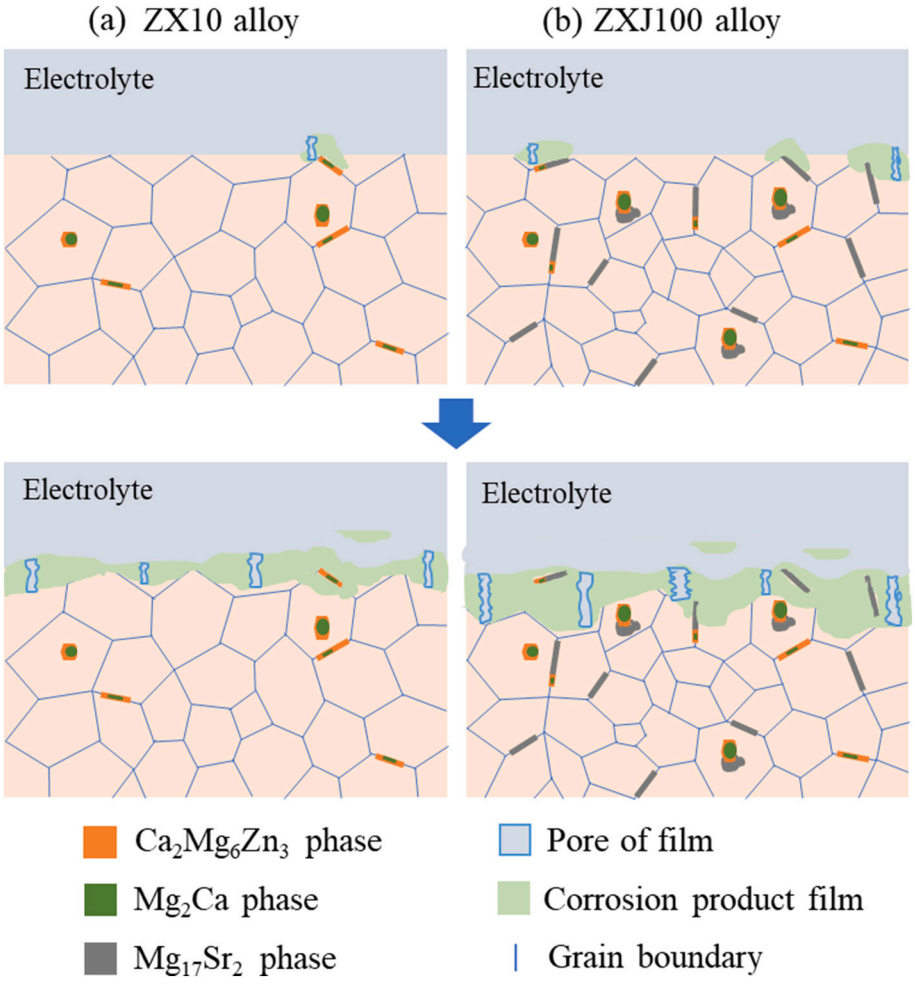

Fig. 13. Schematic illustration of Sr addition on the microstructure and corrosion process of the Mg-Zn-Ca alloy.

the ZX10 alloy. The corrosion resistance of the ZX10 alloy increased monotonously with immersion time, while that of the ZXJ100 alloy exhibited a concave downward trend.

3) The higher corrosion rate of the ZXJ100 alloy was mainly attributed to the more populous micro-galvanic couples formed between the α-Mg matrix and the secondary phases.

CRediT authorship contribution statement

Jun Song: Methodology, Writing – original draft. **Yonghao Gao:** Funding acquisition, Formal analysis, Methodology, Investigation. **Chuming Liu:** Project administration, Conceptualization. **Zhiyong Chen:** Supervision.

Declaration of competing interest

The authors declare that they have no known competing financial interests or personal relationships that could have appeared to influence the work reported in this paper.

Acknowledgments

This work was supported by the Natural Science Foundation of Hunan Province (2019JJ50787) and the Open Sharing Fund for the Large-scale Instruments and Equipments of Central South University (CSUZC202006).

References

[1] J.H. Zhang, S.J. Liu, R.Z. Wu, et al., Recent developments in high-strength Mg-RE-based alloys: focusing on Mg-Gd and Mg-Y systems, J. Magnes. Alloy. 6 (2018) 277–291, https://doi.org/10.1016/j.jma.2018.08.001.
[2] P.-Y. Chen, J. McKittrick, M.A. Meyers, Biological materials: functional adaptations and bioinspired designs, Prog. Mater. Sci. 57 (2012) 1492–1704, https://doi.org/10.1016/j.pmatsci.2012.03.001.
[3] E. Karakulak, A review: past, present and future of grain refining of magnesium castings, J. Magnes. Alloy. 7 (2019) 355–369, https://doi.org/10.1016/j.jma.2019.05.001.
[4] L. Prince, M.A. Rousseau, X. Noirfalise, et al., Inhibitive effect of sodium carbonate on corrosion of AZ31 magnesium alloy in NaCl solution, Corros. Sci. 179 (2021), 109131, https://doi.org/10.1016/j.corsci.2020.109131.
[5] P.F. Ding, Y.C. Liu, X.H. He, et al., In vitro and in vivo biocompatibility of Mg–Zn–Ca alloy operative clip, Bioact. Mater. 4 (2019) 236–244, https://doi.org/10.1016/j.bioactmat.2019.07.002.
[6] E. Zhang, L. Yang, J. Xu, et al., Microstructure, mechanical properties and bio-corrosion properties of Mg–Si(–Ca, Zn) alloy for biomedical application, Acta Biomater. 6 (2010) 1756–1762, https://doi.org/10.1016/j.actbio.2009.11.024.
[7] N. Li, Y.F. Zheng, Novel magnesium alloys developed for biomedical application: a review, J. Mater. Sci. Technol. 29 (2013) 489–502, https://doi.org/10.1016/j.jmst.2013.02.005.
[8] M. Taheri, R.C. Phillips, J.R. Kish, et al., Analysis of the surface film formed on Mg by exposure to water using a FIB cross-section and STEM–EDS, Corros. Sci. 59 (2012) 222–228, https://doi.org/10.1016/j.corsci.2012.03.001.
[9] S.A. Abdel-Gawad, M.A. Shoeib, Corrosion studies and microstructure of Mg−Zn−Ca alloys for biomedical applications, Surf. Interfaces 14 (2019) 108–116, https://doi.org/10.1016/j.surfin.2018.11.011.
[10] H. Wu, C. Zhang, T. Lou, et al., Crevice corrosion – a newly observed mechanism of degradation in biomedical magnesium, Acta Biomater. 98 (2019) 152–159, https://doi.org/10.1016/j.actbio.2019.06.013.
[11] K.B. Nie, Z.H. Zhu, P. Munroe, et al., The effect of Zn/Ca ratio on the microstructure, texture and mechanical properties of dilute Mg-Zn-Ca-Mn alloys that exhibit superior strength, J. Mater. Sci. 55 (2020) 3588–3604, https://doi.org/10.1007/s10853-019-04174-4.

[12] N. Pulido-Gonzalez, B. Torres, S. Garcia-Rodriguez, et al., Mg-1Zn-1Ca alloy for biomedical applications. Influence of the secondary phases on the mechanical and corrosion behaviour, J. Alloys Compd. 831 (2020), 154735, https://doi.org/10.1016/j.jallcom.2020.154735.
[13] G.L. Song, A. Atrens, Understanding magnesium corrosion—a framework for improved alloy performance, Adv. Eng. Mater. 5 (2003) 837–858, https://doi.org/10.1002/adem.200310405.
[14] H. Azzeddine, A. Hanna, A. Dakhouche, et al., Impact of rare-earth elements on the corrosion performance of binary magnesium alloys, J. Alloys Compd. 829 (2020), 154569, https://doi.org/10.1016/j.jallcom.2020.154569.
[15] Y. Chen, L. Wu, W. Yao, et al., A self-healing corrosion protection coating with graphene oxide carrying 8-hydroxyquinoline doped in layered double hydroxide on a micro-arc oxidation coating, Corros. Sci. 194 (2022), 109941, https://doi.org/10.1016/j.corsci.2021.109941.
[16] G. Zhang, L. Wu, A. Tang, et al., Active corrosion protection by a smart coating based on a MgAl-layered double hydroxide on a cerium-modified plasma electrolytic oxidation coating on Mg alloy AZ31, Corros. Sci. 139 (2018) 370–382, https://doi.org/10.1016/j.corsci.2018.05.010.
[17] X.N. Ly, S. Yang, Influence of current mode on microstructure and corrosion behavior of micro-arc oxidation (MAO) biodegradable Mg-Zn-Ca alloy in Hank's solution, Surf. Coat. Technol. 358 (2019) 331–339, https://doi.org/10.1016/j.surfcoat.2018.11.040.
[18] H. Fang, C.X. Wang, S.C. Zhou, et al., Exploration of the enhanced performances for silk fibroin/sodium alginate composite coatings on biodegradable Mg−Zn−Ca alloy, J. Magnes. Alloy. 9 (2021) 1578–1594, https://doi.org/10.1016/j.jma.2020.08.017.
[19] T.S.N. Sankara Narayanan, I.S. Park, M.H. Lee, Strategies to improve the corrosion resistance of microarc oxidation (MAO) coated magnesium alloys for degradable implants: prospects and challenges, Prog. Mater. Sci. 60 (2014) 1–71, https://doi.org/10.1016/j.pmatsci.2013.08.002.
[20] D. Gastaldi, V. Sassi, L. Petrini, et al., Continuum damage model for bioresorbable magnesium alloy devices — application to coronary stents, J. Mech. Behav. Biomed. Mater. 4 (2011) 352–365, https://doi.org/10.1016/j.jmbbm.2010.11.003.
[21] V.S. Saji, Review of rare-earth-based conversion coatings for magnesium and its alloys, J. Mater. Res. Technol. 8 (2019) 5012–5035, https://doi.org/10.1016/j.jmrt.2019.08.013.
[22] M. Deng, L. Wang, D. Höche, et al., Approaching “stainless magnesium” by Ca micro-alloying, Mater. Horiz. 8 (2021) 589–596, https://doi.org/10.1039/D0MH01380C.
[23] C. Zhang, L. Wu, H. Liu, et al., Microstructure and corrosion behavior of Mg-Sc binary alloys in 3.5 wt.% NaCl solution, Corros. Sci. 174 (2020), 108831, https://doi.org/10.1016/j.corsci.2020.108831.
[24] M. Cihova, E. Martinelli, P. Schmutz, et al., The role of zinc in the biocorrosion behavior of resorbable Mg–Zn–Ca alloys, Acta Biomater. 100 (2019) 398–414, https://doi.org/10.1016/j.actbio.2019.09.021.
[25] J.-W. Lee, H.-S. Han, K.-J. Han, et al., Long-term clinical study and multiscale analysis of in vivo biodegradation mechanism of Mg alloy, PANS. 113 (2016) 716–721, https://doi.org/10.1073/pnas.1518238113.
[26] J. Braux, F. Velard, C. Guillaume, et al., A new insight into the dissociating effect of strontium on bone resorption and formation, Acta Biomater. 7 (2011) 2593–2603, https://doi.org/10.1016/j.actbio.2011.02.013.
[27] X. Meng, Z. Jiang, S. Zhu, et al., Effects of Sr addition on microstructure, mechanical and corrosion properties of biodegradable Mg–Zn–Ca alloy, J. Alloys Compd. 838 (2020), 155611, https://doi.org/10.1016/j.jallcom.2020.155611.
[28] H. Pan, K. Pang, F. Cui, et al., Effect of alloyed Sr on the microstructure and corrosion behavior of biodegradable Mg-Zn-Mn alloy in Hanks’ solution, Corros. Sci. 157 (2019) 420–437, https://doi.org/10.1016/j.corsci.2019.06.022.
[29] M.S. Dargusch, Z. Shi, H. Zhu, et al., Microstructure modification and corrosion resistance enhancement of die-cast Mg-Al-Re alloy by Sr alloying, J. Magnes. Alloy. 9 (2021) 950–963, https://doi.org/10.1016/j.jma.2020.09.008.
[30] G.L. Song, A. Atrens, D. John, An hydrogen evolution method for the estimation of the corrosion rate of magnesium alloys, Magnes. Technol. 2001 (2001) 255–262, https://doi.org/10.1002/9781118805497.ch44.
[31] T. Zhou, D. Chen, Z.-h. Chen, Microstructures and properties of rapidly solidified Mg-Zn-Ca alloys, Trans. Nonferrous Metals Soc. China 18 (2008) s101–s106, https://doi.org/10.1016/S1003-6326(10)60183-5.
[32] G. Baril, G. Galicia, C. Deslouis, et al., An impedance investigation of the mechanism of pure magnesium corrosion in sodium sulfate solutions, J. Electrochem. Soc. 154 (2007) C108, https://doi.org/10.1149/1.2401056.
[33] M. Bornapour, N. Muja, D. Shum-Tim, et al., Biocompatibility and biodegradability of Mg–Sr alloys: the formation of Sr-substituted hydroxyapatite, Acta Biomater. 9 (2013) 5319–5330, https://doi.org/10.1016/j.actbio.2012.07.045.
[34] J.H. Nordlien, S. Ono, N. Masuko, et al., A TEM investigation of naturally formed oxide films on pure magnesium, Corros. Sci. 39 (1997) 1397–1414, https://doi.org/10.1016/S0010-938X(97)00037-1.
[35] D.E. Haycock, M. Kasrai, C.J. Nicholls, et al., The electronic structure of magnesium hydroxide (brucite) using X-ray emission, X-ray photoelectron, and auger spectroscopy, J. Chem. Soc. Dalton Trans. (1978) 1791–1796, https://doi.org/10.1039/DT9780001791.
[36] C.D. Wagner, D.A. Zatko, R.H. Raymond, Use of the oxygen KLL Auger lines in identification of surface chemical states by electron spectroscopy for chemical analysis, Anal. Chem. 52 (1980) 1445–1451, https://doi.org/10.1021/ac50059a017.
[37] A.L. Rudd, C.B. Breslin, F. Mansfeld, The corrosion protection afforded by rare earth conversion coatings applied to magnesium, Corros. Sci. 42 (2000) 275–288, https://doi.org/10.1016/S0010-938X(99)00076-1.
[38] Z. Shi, A. Atrens, An innovative specimen configuration for the study of Mg corrosion, Corros. Sci. 53 (2011) 226–246, https://doi.org/10.1016/j.corsci.2010.09.016.
[39] M.P. Gomes, I. Costa, N. Pébère, et al., On the corrosion mechanism of Mg investigated by electrochemical impedance spectroscopy, Electrochim. Acta 306 (2019) 61–70, https://doi.org/10.1016/j.electacta.2019.03.080.
[40] J.R. Li, Q.T. Jiang, H.Y. Sun, et al., Effect of heat treatment on corrosion behavior of AZ63 magnesium alloy in 3.5wt.% sodium chloride solution, Corros. Sci. 111 (2016) 288–301, https://doi.org/10.1016/j.corsci.2016.05.019.
[41] F. Mansfeld, M.W. Kendig, S. Tsai, Evaluation of corrosion behavior of coated metals with AC impedance measurements, Corrosion. 38 (1982) 478–485, https://doi.org/10.5006/1.3577363.
[42] F. Mansfeld, Use of electrochemical impedance spectroscopy for the study of corrosion protection by polymer coatings, J. Appl. Electrochem. 25 (1995) 187–202, https://doi.org/10.1007/BF00262955.
[43] G. Baril, N. Pébère, The corrosion of pure magnesium in aerated and deaerated sodium sulphate solutions, Corros. Sci. 43 (2001) 471–484, https://doi.org/10.1016/S0010-938X(00)00095-0.
[44] G. Song, A. Atrens, D.S. John, et al., The anodic dissolution of magnesium in chloride and sulphate solutions, Corros. Sci. 39 (1997) 1981–2004, https://doi.org/10.1016/S0010-938X(97)00090-5.
[45] K.D. Ralston, N. Birbilis, Effect of grain size on corrosion: a review, Corrosion 66 (2010), https://doi.org/10.5006/1.3462912, 075005-075005-075013.
[46] Y. Lu, A.R. Bradshaw, Y.L. Chiu, et al., Effects of secondary phase and grain size on the corrosion of biodegradable Mg-Zn-Ca alloys, Mater. Sci. Eng. C 48 (2015) 480–486, https://doi.org/10.1016/j.msec.2014.12.049.
[47] N.T. Kirkland, N. Birbilis, J. Walker, et al., In-vitro dissolution of magnesium–calcium binary alloys: clarifying the unique role of calcium additions in bioresorbable magnesium implant alloys, J. Biomed. Mater. Res. B 95B (2010) 91–100, https://doi.org/10.1002/jbm.b.31687.
[48] Y.H. Gao, A. Yerokhin, A. Matthews, Effect of current mode on PEO treatment of magnesium in Ca- and P-containing electrolyte and resulting coatings, Appl. Surf. Sci. 316 (2014) 558–567, https://doi.org/10.1016/j.apsusc.2014.08.035.
[49] A.D. King, N. Birbilis, J.R. Scully, Accurate electrochemical measurement of magnesium corrosion rates; a combined impedance, mass-loss and hydrogen collection study, Electrochim. Acta 121 (2014) 394–406, https://doi.org/10.1016/j.electacta.2013.12.124.